

# Aero-Optic Effects of a Wing Tip Vortex

Chris Porter<sup>1</sup>, Mark Rennie<sup>2</sup>, and Eric Jumper<sup>3</sup>  
*University of Notre Dame, Notre Dame, Indiana, 46545*

For an airborne optical system carried by a helicopter, aero-optic aberrations originate primarily from blade tip vortices that pass through the system field of view; these aberrations result from the reduced pressure and density in the vortex cores and the associated variations in the index-of-refraction. Using the weakly compressible model (WCM) previously developed at Notre Dame, aero-optic effects for realistic tip-vortex flows are computed using the Lamb-Oseen vortex model as well as experimental velocity fields, and compared to measured wavefronts. Scaling relations are developed that enable the prediction of the aero-optic aberrations for full-scale flight vehicles.

## Nomenclature

$AP$	=	aperture ratio
$AR$	=	aspect ratio
$c$	=	chord
$C_p$	=	specific heat (at constant pressure)
$G$	=	aperture gain function
$M$	=	Mach number
$n$	=	index of refraction
$OPD$	=	optical path difference
$P$	=	pressure
$P_s$	=	static pressure
$r_c$	=	vortex core radius
$\bar{r}$	=	non-dimensional radius, normalized by the vortex core radius
$T$	=	temperature
$t$	=	time
$T_{AD}$	=	adiabatic temperature
$T_o$	=	total temperature
$u$	=	streamwise velocity component
$v$	=	spanwise velocity component
$\vec{V}$	=	velocity vector
$V_x$	=	axial velocity
$V_\theta$	=	tangential velocity
$w$	=	vertical velocity component
$\Gamma$	=	circulation
$\gamma$	=	ratio of specific heats
$\rho$	=	density

## I. Introduction

THE aero-optic environment around optical systems mounted on high-speed transports and combat aircraft has received considerable attention [1-5]. These efforts have included investigations into the optical aberrations caused by compressible boundary-layer [1] and shear-layer flows [2], in addition to studies of the aero-optics associated with complete turret assemblies [3, 4]. In general, the goal of these studies is to determine methods to correct or mitigate the effects of optically-active flows [5].

<sup>1</sup> Graduate Student, Department of Aerospace and Mechanical Engineering, Student Member AIAA.

<sup>2</sup> Research Assistant Professor, Department of Aerospace and Mechanical Engineering, Senior Member AIAA.

<sup>3</sup> Professor, Department of Aerospace and Mechanical Engineering, Fellow AIAA.

For helicopter-mounted optical systems, the flight speed of the aircraft platform is in most cases, incompressible; as such, aero-optic aberrations are expected to originate primarily from the helicopter blades which can have tip speeds up to Mach 1 in some parts of the flight envelope. Evaluating the aero-optic environment in the vicinity of the helicopter therefore depends upon an understanding of the blade wake and tip-vortex dynamics and its associated aero-optic aberrations, as well as an understanding of the character of the helicopter gross flow field in order to determine the location of the blade wake system as a function of helicopter flight regime. To the knowledge of the authors, no such investigation has been previously performed. As a first step towards an understanding of the detailed aero-optic environment for helicopter-mounted optical systems, this paper presents an experimental investigation into the aero-optic effects caused by helicopter-blade tip vortices.

## II. Approach

The fluid mechanics of wing-tip vortices has been studied extensively in the past since they dominate the wakes of lifting vehicles and have a direct impact on aircraft spacing near airports [6-10]. These studies show that the tip-vortex flow field consists of a rotational core surrounded by an irrotational outer region. The core region of the vortex may also contain either jet-like or wake-like axial velocity components depending on the particular origin and history of the vortex. Since the total pressure is nearly constant across the vortex profile, the large flow velocities (both axial as well as azimuthal) close to the vortex core result in a significant reduction in static pressure at the center of the vortex; it is this reduced static pressure at the center of the vortex, with concomitant reductions in density and index of refraction, that result in the aero-optic aberrations produced by a tip vortex. Although the global wake structure for a helicopter may be significantly different from that for fixed-wing aircraft (i.e. helical tip vortex pattern versus a linear one), the flow field for a single tip vortex is essentially the same, with vortices shed from both types of aircraft showing good agreement with, for example, the Lamb-Oseen vortex model.

The kinds of tip-vortex aero-optic aberrations described above could be considered to be fluid mechanic in origin in the sense that index-of-refraction variations ultimately originate from the velocity field of the tip vortex. As shown in [11], at low-convective Mach numbers, the velocity field is unaffected by the thermodynamic properties of the flow. In this case, an existing empirical or experimental velocity field can be used to immediately determine the pressure, temperature, and density fields, which can be used to calculate the optical aberrations induced by the flow. A fluid-dynamic model that performs this computation, called the weakly compressible model (WCM), has been developed previously at the University of Notre Dame [12], and is outlined in the following brief description.

The WCM is designed to compute pressure, temperature, and density fields from a pre-determined velocity field for “weakly compressible” flows in which development of the velocity field can be assumed to be decoupled from thermodynamic properties. The model is composed of the unsteady Euler equations, an isentropic temperature relation, and the ideal gas law:

$$\begin{aligned} Du/Dt &= \partial u/\partial t + u \partial u/\partial x + v \partial u/\partial y + w \partial u/\partial z \\ Dv/Dt &= \partial v/\partial t + u \partial v/\partial x + v \partial v/\partial y + w \partial v/\partial z \\ Dw/Dt &= \partial w/\partial t + u \partial w/\partial x + v \partial w/\partial y + w \partial w/\partial z \end{aligned} \quad (1)$$

The pressure gradients can then be calculated using Euler’s equation

$$\begin{aligned} \partial P/\partial x &= -\rho Du/Dt \\ \partial P/\partial y &= -\rho Dv/Dt \\ \partial P/\partial z &= -\rho Dw/Dt \end{aligned} \quad (2)$$

The solution is started by setting the initial guess for the pressure field as  $p(x,y,z) = p_\infty$ , after which Eqs. (1) to (4) are iterated to convergence. The initial adiabatic temperature distribution  $T_{AB}$  is computed using an assumed initial constant total temperature throughout the flow field. The final  $T_T$  distribution of the converged solution can, however, vary throughout the flow field due to local unsteady pressure variations.

$$T_S = T_{Ad} \left( P/P_\infty \right)^{\gamma-1/\gamma} \quad (3)$$

$$P = \rho RT_s \quad (4)$$

In Eq. (3), the adiabatic static temperature distribution,  $T_{Ad}$ , is determined at each point in the field using the velocity field by Eq. (5). Once the density field has been determined using the WCM, the index of refraction  $n$  at each point in the flow is determined using Eq. (6).

$$T_{Ad} = T_o - \frac{\bar{V}^2}{2C_p} \quad (5)$$

$$n(x, y, z) = 1 - K_{GD}\rho(x, y, z) \quad (6)$$

In Eq. (6), the Gladstone-Dale constant for 1  $\mu\text{m}$  wavelength radiation in air is  $K_{GD} = 2.25 \times 10^{-3} \text{ kg/m}^3$ . Finally, the optical path difference, OPD, at each point of a beam of light passing through the index-of-refraction field is given by:

$$OPD = OPL - \overline{OPL} \quad (7)$$

$$OPL = \int n(t, x, y, z) dy \quad (8)$$

The approach for the present study was to determine aero-optic aberrations for realistic tip-vortex flows using the WCM in conjunction with empirical or experimental data for vortex velocity fields. As mentioned above, the resulting aero-optic data can be considered to be fluid mechanic in origin. Thermal aberrations could also be produced if temperature variations in the flow produced significant index-of-refraction gradients; such thermal aberrations would result, for example, if the helicopter engine exhaust were convected into the line of sight of the helicopter-mounted optical system. Effective treatment of such thermal aberrations requires, however, detailed computation or measurement of the flow and sources of heat around the helicopter and is beyond the scope of the present study.

### III. Results

#### A. Example of Aero-Optic Aberrations Due to a Tip Vortex

Since wing-tip vortex flow fields are self-similar and compressibility effects on the flow field are small, the aero-optic character of a wing-tip vortex was estimated using the WCM in conjunction with a flow field that was scaled from subsonic measurements [13]. These measurements were performed on an unswept wing with a NACA 0012 profile, a chord of 0.127 m, and an aspect ratio of 8. At a distance of four chords downstream of the trailing edge of the wing, three component hot-wire measurements were made over a grid of 0.076 x 0.076 meters in 0.0025 meter increments in the y and z directions. This velocity field was then normalized by the freestream velocity and then scaled to different freestream Mach numbers.

Figure 1 shows the non-dimensional velocity field obtained from the hot wire measurements and the corresponding vorticity contours. In Fig. 2, the experimental velocity field is compared to an estimate of the velocity field produced using the Lamb-Oseen model [10, 14]:

$$V_\theta(\bar{r}) = \frac{\Gamma}{2\pi r_c \bar{r}} (1 - e^{-\alpha \bar{r}^2}). \quad (9)$$

$$V_x = -\frac{A}{x} e^{-\alpha \bar{r}^2}. \quad (10)$$

As shown by Eqs. (9) and (10), the velocity field of the Lamb-Oseen tip vortex is determined by the vortex core radius ( $r_c$ ), the circulation ( $\Gamma$ ), and the strength of the wake axial velocity profile ( $A$ ); in Fig. 2, these parameters were selected to match the experimental data. Figure 2 shows that the experimental data can be accurately characterized by the Lamb-Oseen model.

The experimental velocity field was next scaled to  $M=0.3$ . The pressure and temperature fields, as well as the aero-optic aberration associated with this scaled experimental velocity field were computed using the WCM, shown in Figs. 3 and 4. As shown in Fig. 4, the peak-to-peak difference in OPD due to the  $M=0.3$  vortex aberration is  $0.25 \mu\text{m}$ . This aberration would have a significant impact on a  $1 \mu\text{m}$  wavelength beam of light that traversed the vortex flow field. It should be noted, however, that the results shown in Figs. 3 and 4 are for a relatively small tip vortex produced by a  $0.127 \text{ m}$  chord wing at  $M=0.3$ . The aberrations produced by full-scale helicopter blade with significantly larger length scales, aerodynamic loading, and Mach number could produce significantly larger aberrations. Relations to scale the reduced-scale experimental to full-scale results are developed in the following section.

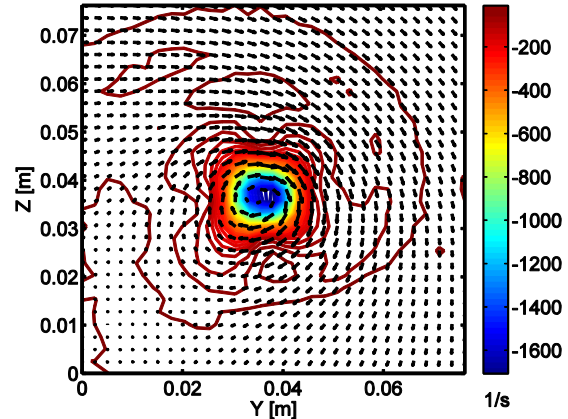


Fig. 1. Non-dimensional velocity field for a wing tip vortex at 4 chord lengths downstream of the wing tip [13].

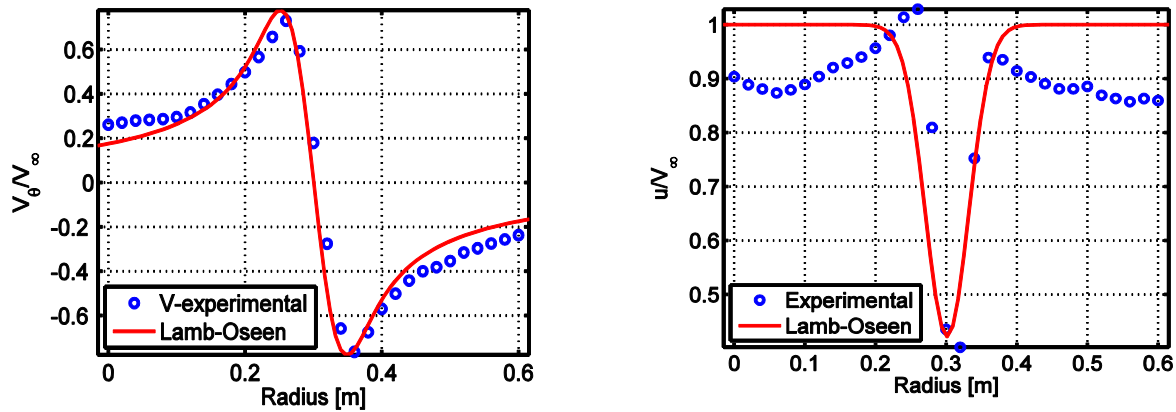


Fig. 2. Comparison of Lamb-Oseen vortex model with three-component hotwire data [13].

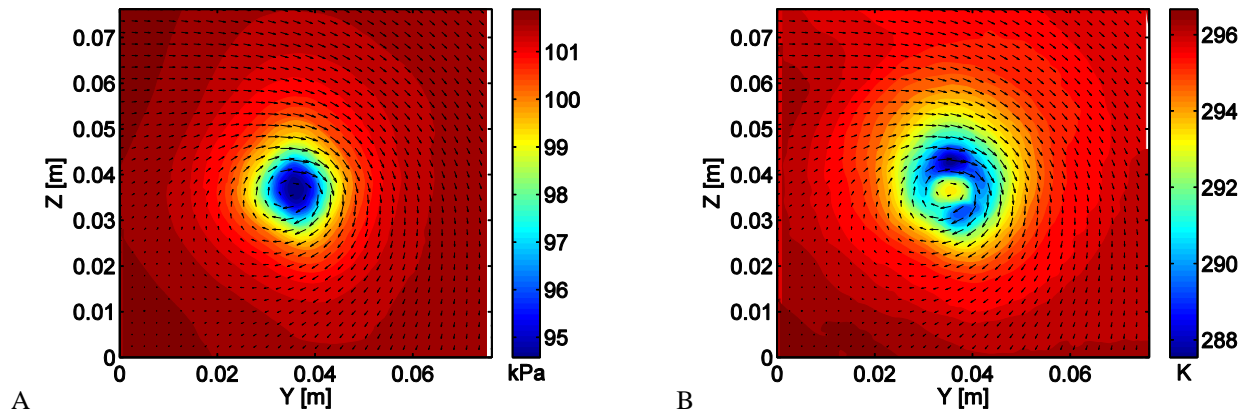


Fig. 3. Pressure (A) and temperature (B) fields computed using the WCM for an experimental tip-vortex velocity field scaled to  $M=0.3$ .

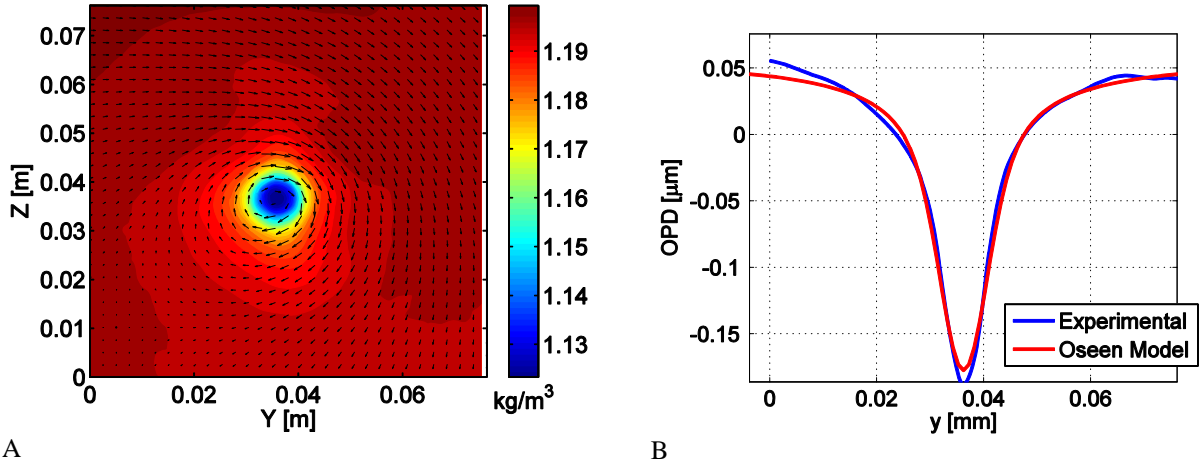


Fig. 4. (A) WCM-computed density field for scaled experimental tip-vortex data and, (B) the corresponding OPD for the experimental data and the Lamb-Oseen model.

## B. Scaling Relations

Scaling relations for the optical aberrations due to a tip vortex are developed from the Euler equations and the assumptions that there is no radial velocity component and that the vortex is axisymmetric:

$$\begin{aligned} \frac{V_\theta}{r} &= \frac{1}{\rho} \frac{\partial P}{\partial r} \\ V_x \frac{\partial V_x}{\partial x} &= -\frac{1}{\rho} \frac{\partial P}{\partial x} \\ \frac{\partial P}{\partial \theta} &= 0 \end{aligned} \quad (11)$$

Dimensional analysis of Eqs. (11) shows that the pressure gradient in the radial direction is approximately an order of magnitude larger than the pressure gradient in the streamwise direction [14]. As such, if the axial flow equation (second equation in Eq. (11)) is neglected, then inserting Eq. (9) into Eq. (11) gives:

$$\frac{\Gamma^2}{4\pi r^3} \left( 1 - e^{-2a\left(\frac{r}{r_c}\right)^2} \right) = \frac{1}{\rho} \frac{\partial P}{\partial r}. \quad (12)$$

For isentropic flow, the right hand side of Eq. (12) becomes:

$$\frac{1}{\rho} \frac{\partial P}{\partial r} = \frac{\gamma RT}{\rho} \frac{\partial \rho}{\partial r}. \quad (13)$$

Substituting Eq. (13) into Eq. (12) and integrating to obtain the density, then computing the index-of-refraction (Eq. (6)) and integrating as shown in Eq. (8), the OPD is seen to scale as:

$$OPD_{RMS} \sim \left( \frac{\rho}{\rho_{SL}} \right) \frac{\Gamma^2}{a^2 r_c} \quad (14)$$

where  $a$  is the speed of sound. Assuming that the circulation of the vortex is equal to the circulation associated with the wing lift, the scaling relation Eq. (14) can also be expressed as:

$$OPD_{RMS} \sim \left( \frac{\rho}{\rho_{SL}} \right) \frac{C_l^2 M^2 c^2}{r_c}. \quad (15)$$

Based on this scaling, the spatial  $OPD_{RMS}$  is a function of the lift coefficient, Mach number, chord length, and vortex core radius. This indicates that if the lift from the wing decreases, so will the  $OPD_{RMS}$ , eventually going to zero as the lift goes to zero. Furthermore, the same Mach number squared relationship found in boundary layer experiments [15] is also obtained, and once again as the freestream Mach number goes to zero so does the  $OPD_{RMS}$ . Finally, if the vortex diffuses due to viscous effects as predicted in the Lamb-Oseen model, or if vortex breakdown occurs, then Eq. (15) shows that the resulting increase in the core radius of the vortex produces a reduction in the overall spatial  $OPD_{RMS}$ .

The scaling relations shown in Eqs. (14) and (15) were developed from an analysis of basic fluid-mechanic equations. To investigate the relations a data base of the optical aberrations for a range of tip-vortex parameters was generated. These data were created by generating velocity fields using the Lamb-Oseen model (Eqs. (9) and (10)), determining the associated index-of-refraction field using the WCM, and computing the spatial  $OPD_{RMS}$  associated with a collimated beam that traverses the flow field. Optical data were also generated, in a similar way, by scaling the experimental flow field of [13] to different Mach numbers. Figure 5A shows these data plotted as a function of Mach number. In Fig. 5B, the same data are plotted as a function of the scaling parameter  $(\rho/\rho_{sl}) \Gamma/a^2 r_c$  shown in Eq. (14); Fig. 5B shows that this scaling parameter successfully collapses the data onto a single curve.

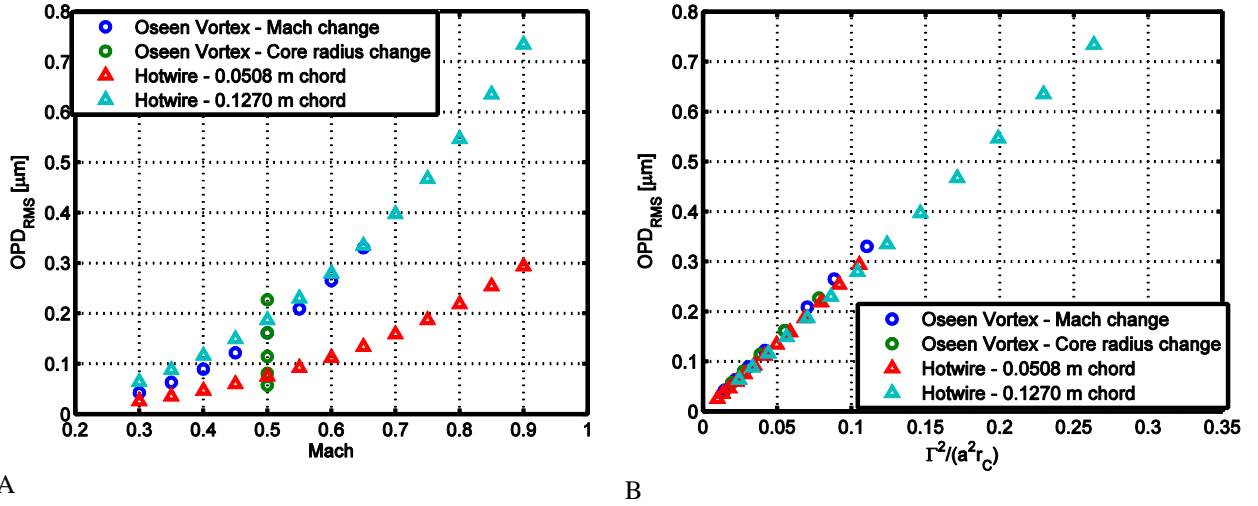


Fig. 5. (A) Optical aberrations computed using the WCM for various tip-vortex parameters and, (B) the data scaled data according to Eq. (14).

For the data shown in Fig. 5A, the vortex velocity fields were effectively two-dimensional in the sense that the axial velocity components were zero or very small. In reality, the tip-vortex velocity field typically includes a wake-like or jet-like axial velocity component. As such, a second data base of tip-vortex optical aberrations were computed using the Lamb-Oseen model, this time with different values of the wake parameter  $A$  in Eq. (10). As shown in Fig. 6A, these data collapse onto slightly different curves when plotted against the scaling parameter of Eq. (14). This indicates that the axial velocity field has a small but significant effect on the scaling of optical aberrations caused by the tip vortex. To account for this effect, a second scaling relation for the optical aberrations due to the vortex axial flow field was determined by substituting the Lamb-Oseen axial-velocity relation Eq. (10) into Eq. (11), this time neglecting the radial pressure gradient, and integrating as before:

$$OPD_{RMS} \sim \left( \frac{\rho}{\rho_{SL}} \right) \frac{A^2 r_c}{a^2 x^2}. \quad (16)$$

If it is assumed that the aberrations due the radial and axial velocity components are independent, then an overall scaling relation for the aberrations due to a tip vortex can be obtained by adding Eqs. (14) and (16):

$$OPD_{RMS} \sim C_1 \left( \frac{\rho}{\rho_{SL}} \right) \left( \frac{r_c}{a^2} \right) \left( \left[ \frac{\Gamma}{r_c} \right]^2 + C_2 \left[ \frac{A}{x} \right]^2 \right) \quad (17)$$

where  $C_1$  and  $C_2$  are constants that must be fit to experimental or numerical data. Figure 6B shows the same data from Fig. 6A replotted using the scaling relation Eq. (17). The figure shows that the combined scaling relation,

Eq. (17), collapses all of the data on to a single curve. The constant  $C_2=9.53$  shown in Fig. 6B was determined by minimizing the spread of the data in a least squares sense.

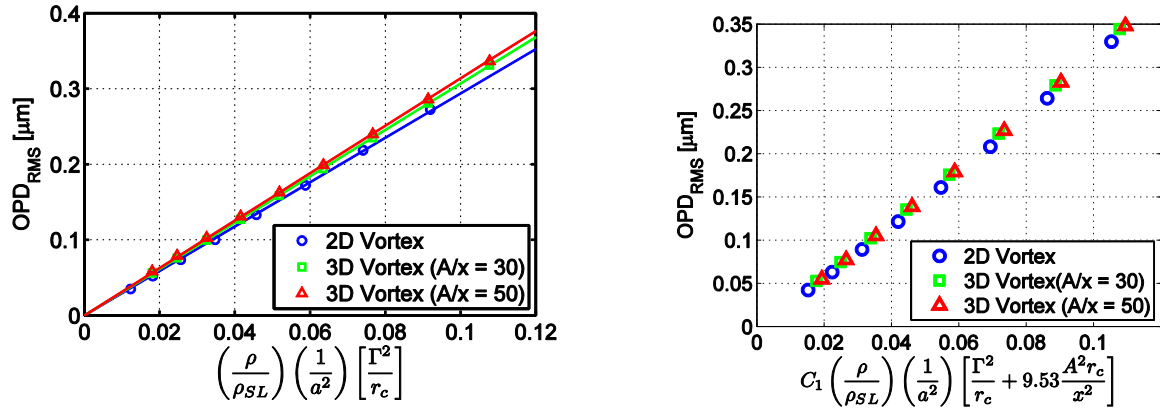


Fig. 6. WCM-computed optical aberrations for tip vortices with both circumferential and axial velocity components.

As shown in Fig. 4B, the aberration produced by a tip vortex is greatest at the location of the vortex core and drops off with radial distance away from the core. As such, the effect of the aberration on a traversing beam of light depends on the diameter of the beam aperture compared to the diameter of the vortex. The beam aperture therefore acts as a spatial gain,  $G(AP)$ , either increasing or decreasing the spatial  $OPD_{RMS}$  as the ratio of the vortex core to the beam aperture changes [16, 17].

The effect that the aperture diameter has on the tip-vortex aberration is investigated in Fig. 7A, which shows the  $OPD_{RMS}$  computed for the same tip-vortex flow field as a function of aperture diameter. As shown in Fig. 7A, a large amount of variability in the  $OPD_{RMS}$  exists when the size of the aperture diameter changes; however, as shown in Fig. 7B, nondimensionalization of the aperture diameter by the vortex core diameter collapses the normalized  $OPD_{RMS}$  data onto a single curve. The curve shown in Fig. 7B can therefore be used to scale tip-vortex  $OPD_{RMS}$  data to different measurement apertures. For example, Fig. 8 shows tip-vortex aberrations computed using the WCM for different Mach numbers and beam apertures. Figure 8A shows the data without any adjustment for the aperture ratio, AP (i.e. aperture diameter to vortex core diameter), while Fig. 8B shows the same data adjusted to the same aperture ratio through the gain function  $G(AP)$  shown in Fig.7B; the figure shows that scaling the data to the same aperture ratio collapses the data onto a single curve. The gain function,  $G(AP)$ , is the ratio of the normalized  $OPD_{RMS}$  for the value of the desired aperture ratio to the current aperture ratio, both of which are obtained from Fig. 7B. In Fig. 8B, all the data were adjusted to an aperture ratio of 10.

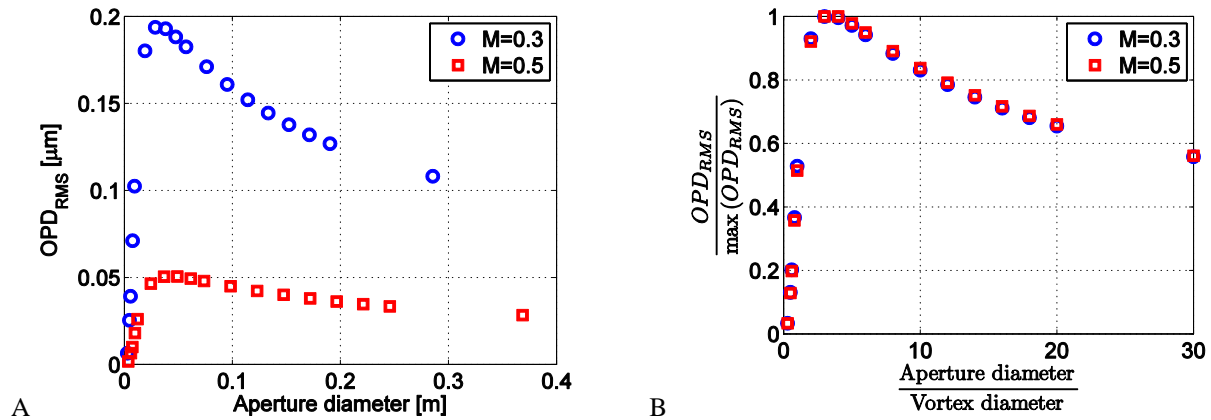
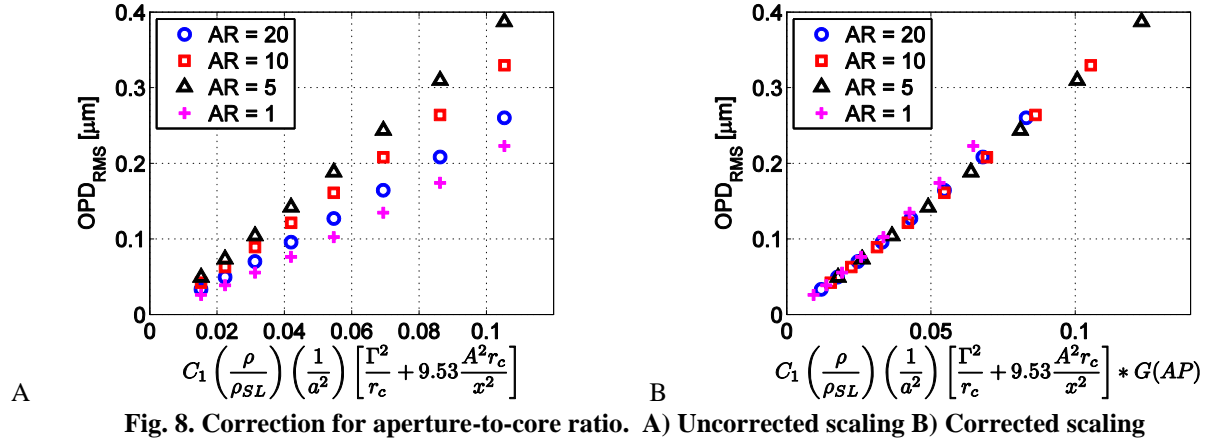


Fig. 7. (A) Effect of aperture diameter on the computed  $OPD_{RMS}$ ; (B) with data nondimensionalized.



In summary, an overall scaling relation that includes aperture effects is shown in Eq. (18), where the aperture scaling function  $G(AP)$  is shown in Fig. 7:

$$OPD_{RMS} \sim C_1 \left( \frac{\rho}{\rho_{SL}} \right) \left( \frac{r_c}{a^2} \right) \left( \left[ \frac{\Gamma}{r_c} \right]^2 + 9.53 \left[ \frac{A}{x} \right]^2 \right) G(AP). \quad (18)$$

Finally, using a least squares approach, the value for  $C_1$  was determined from the Lamb-Oseen data to be 3.1, yielding:

$$OPD_{RMS} = 3.1 \left( \frac{\rho}{\rho_{SL}} \right) \left( \frac{r_c}{a^2} \right) \left( \left[ \frac{\Gamma}{r_c} \right]^2 + 9.53 \left[ \frac{A}{x} \right]^2 \right) G(AP). \quad (19)$$

### C. Experimental Measurements

To verify the WCM results and the scaling relation, Eq. (19), wavefront measurements using a Shack-Hartmann sensor were taken behind a half-span 60 degree delta wing. A 90 mm diameter planar-collimated beam was sent through a 100x100 mm test section at 200 mm downstream of the trailing edge of the delta wing, see Fig. 9. The delta wing was set to three different angles of attack: 5, 10, and 15 degrees, and wavefronts were measured at Mach numbers of 0.3, 0.4, and 0.5. The test-section blockage, based on the frontal area of the wing ranged from 7 to 23%. During each test, 200 wavefronts were acquired at 10 Hz. Figure 10 shows the average OPD from each data set, in which tip/tilt has been removed based on the least squares best fit plane to the data. The trough at center of each image is the wingtip vortex. In each of the figures shown in Fig. 10, the flow is from left to right.

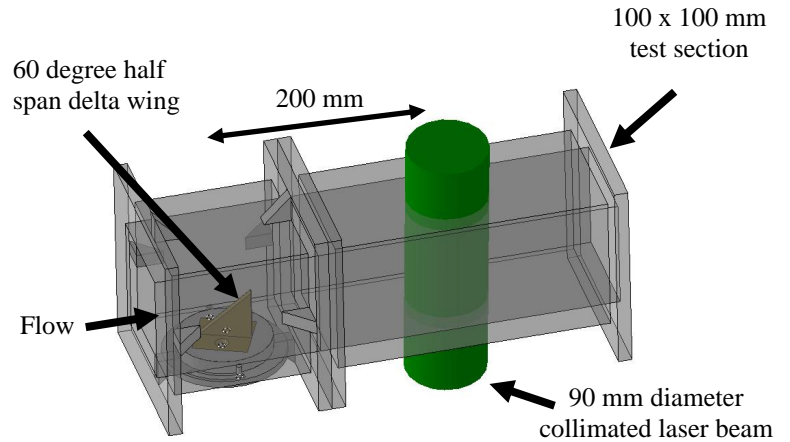
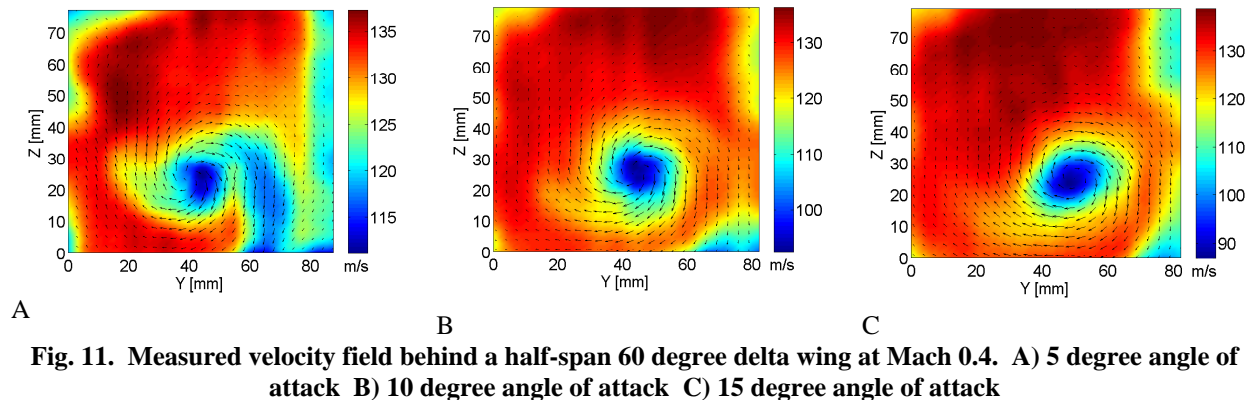
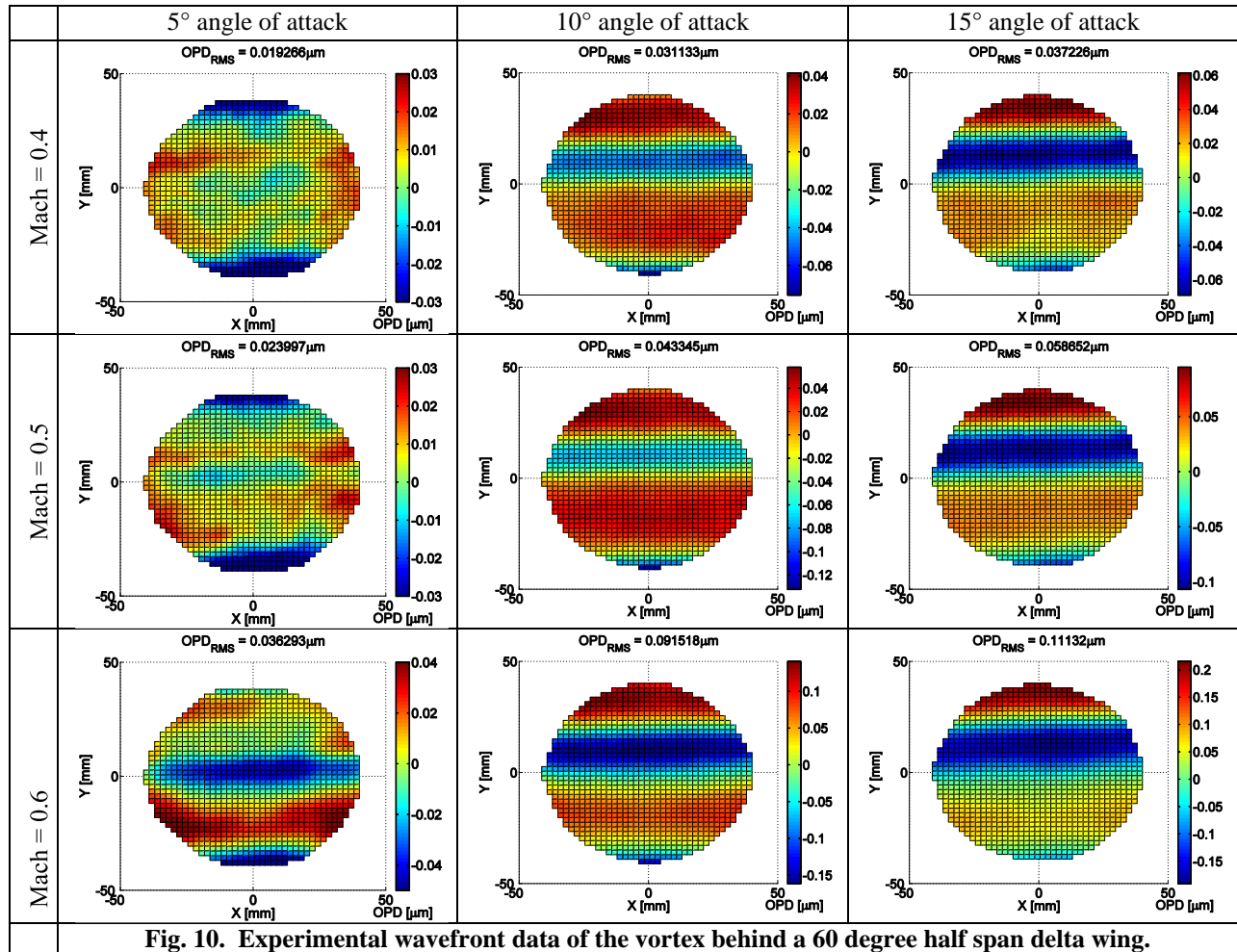


**Fig. 9. Experimental setup**

The velocity field at the location of the wavefront measurements were also measured using a cross-wire. To obtain all three velocity components behind the delta wing the flow was surveyed twice with the cross-wire rotated by 90 degrees between surveys. All the hotwire data were taken at a freestream Mach number of 0.4 for wing angles of attack of 5, 10, and 15 degrees. The results of the cross-wire survey are plotted in Fig. 11, in which the contours represent the U component, and the vectors the V and W components.



The mean velocity field measured using the cross-wire was used to compute the aberration on a traversing beam of light using the WCM. Figure 12 shows that the WCM-computed OPD determined from the mean cross-wire data compares well to the mean OPD measured directly using the wavefront sensor. Figure 12 shows that the aberrations determined from both the WCM and the wavefront sensor do not approach a constant value outside of the core of the vortex, but instead fall off rapidly near the tunnel wall. This drop off is likely due to corner vortices present in the wind-tunnel test section which are clearly visible in Fig. 11. The good comparison between the WCM results and the direct wavefront measurements shown in Fig. 12 provides validation for the data and scaling relation, Eq. (19), obtained using a WCM analysis of vortex velocity fields.

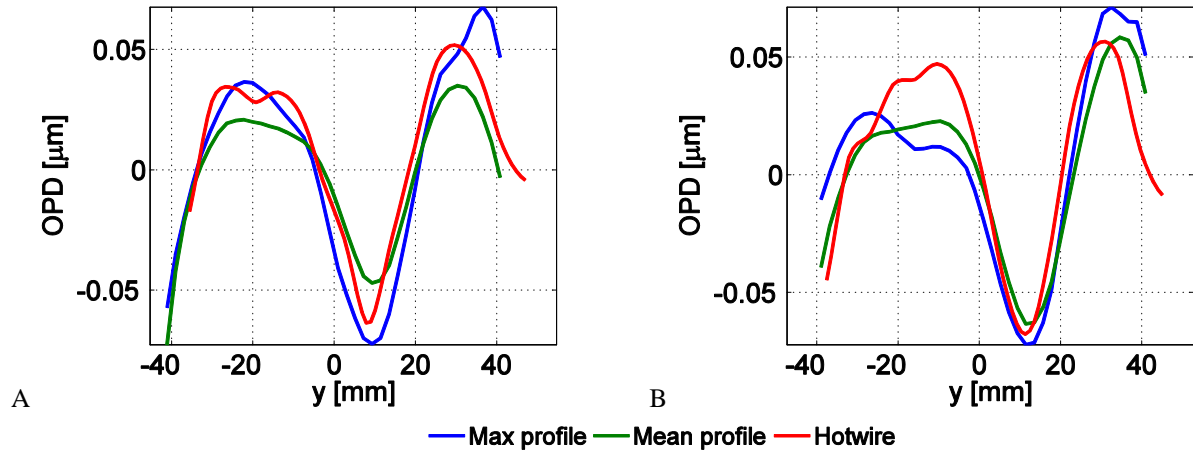


Fig. 12. Comparison of measured wavefront data and WCM-computed wavefronts from cross-wire measurements behind delta wing. A) 10 degree angle of attack B) 15 degree angle of attack

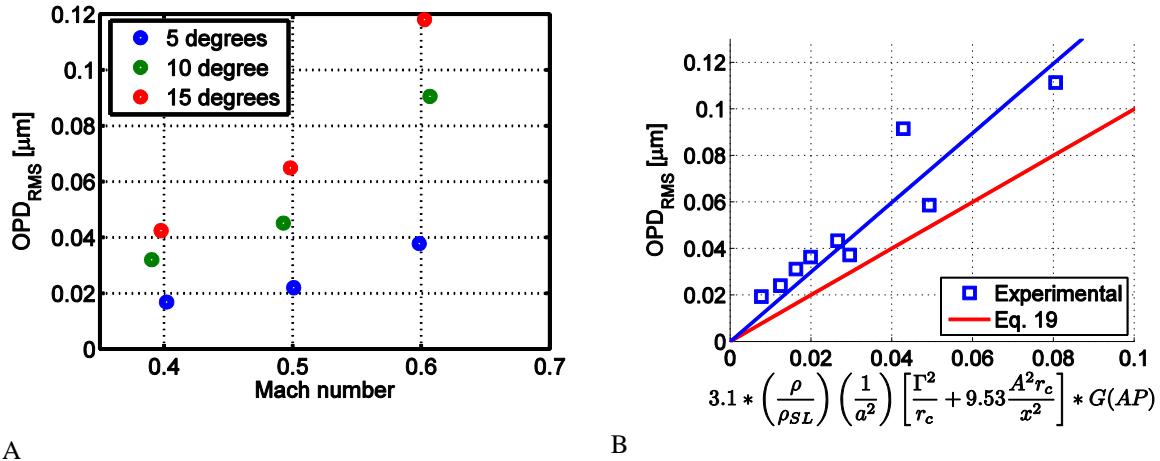


Fig. 13. Measured spatial OPD behind a 60-degree half span delta wing. A) Un-scaled measured spatial OPD. B) Two-dimensional scaling based on Eq. 12 with aperture correction.

The  $OPD_{RMS}$  from the direct wavefront measurements are summarized in Fig. 13A, while Fig. 13B compares these data to the curve fit determined using the WCM in conjunction with Lamb-Oseen velocity fields, Eq. (19). The figure shows that the experimental wavefront data collapse onto a single line with a slightly different slope than Eq. (19), indicating that Eq. (19) accurately models the physics of the experimental results except for a simple multiplicative constant. One possible explanation for this discrepancy is the blockage effects that the tunnel walls had on the experimental wavefront measurements which, as shown in Figs. 11 and 12, resulted in some distortion of the velocity and OPD measurements at the tunnel walls thereby making it difficult to determine accurate values of the  $OPD_{RMS}$  and vortex circulation for comparison with the model, Eq. (19). Additional measurements of the wavefronts and velocity fields of a tip-vortex will be performed in a wind-tunnel with larger cross section; however, Figs. 12 and 13 shows that Eq. (19) still performs reasonably well for modeling tip-vortex  $OPD_{RMS}$ .

#### D. Full-Scale Predictions (UH-60)

Using Eq. (19), predictions of the severity of the aberration from the rotor tip vortices for a full-scale helicopter were made; in this case, the helicopter chosen for the prediction was the UH-60. The strength of the tip vortices was calculated based on the weight (16680 N), number of blades (4), and assuming that all of the circulation associated

with lifting the helicopter is shed into the tip vortex. The calculated blade circulation, using these parameters and assumptions was  $49.8 \text{ m}^2/\text{s}$ . Using Landgrebe's model [14], the tip vortex path was predicted using published data for hovering flight [14] and is shown in Fig. 14. Figure 15 shows the predicted  $\text{OPD}_{\text{RMS}}$  for this configuration as a function of distance  $x$  downstream of the blade tip. For the calculations shown in Fig. 15, the axial-flow parameter  $A$  in Eq. (19) was set to 0 so that the case of no axial velocity in the vortex core was modeled; as such, the predictions shown here are conservative in the sense that the existence of an axial-flow velocity component would serve to increase the predicted  $\text{OPD}_{\text{RMS}}$ . Based on the Landgrebe model, the tip vortex travels approximately 150 to 200 chord lengths before it moves below the helicopter body and into the line of sight of an optical system mounted underneath the helicopter. As shown in Fig. 15, the  $\text{OPD}_{\text{RMS}}$  at a wake distance of 150 chord lengths is approximately  $0.14 \text{ }\mu\text{m}$ . Computation of the Strehl ratio, Eq. (20) for a nominal  $1 \text{ }\mu\text{m}$  wavelength beam gives a value of 0.46; this level of aberration, although not catastrophic, would seriously impede the ability to focus the beam on a farfield target.

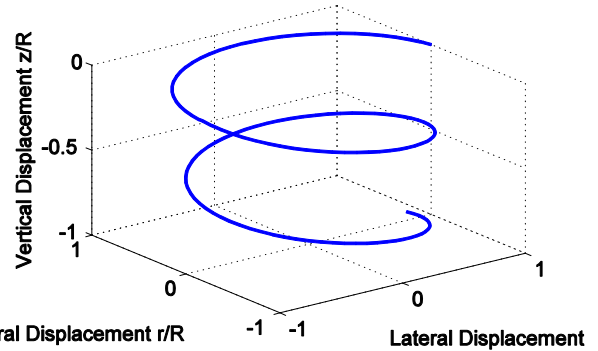


**Fig. 14. Landgrebe model [14] predicting the location of a vortex core for a helicopter on hover.**

$$St = \exp \left[ - \left( \frac{2\pi \text{OPD}_{\text{RMS}}}{\lambda} \right)^2 \right] \quad (20)$$

The results of this full-scale prediction therefore indicate that the passage of a tip vortex through the beam path would seriously degrade the farfield performance of a helicopter-mounted optical system. As shown by Fig. 15, the strength of the tip vortex aberration decays as the tip vortices move downward from the helicopter blades; however, when the helicopter is in hover, the vortex aberrations just below the body of the helicopter are still sufficiently strong to significantly aberrate a traversing beam. This outcome has particularly serious consequences for helicopter-mounted systems if it is recognized that a belly-mounted optical system is most likely to point at distant targets by aiming just below the body of the helicopter. Finally, it should be noted that these full-scale helicopter results were estimated from published data [14], and that if the actual tip vortex radius were only slightly smaller than the aberration produced by the blade vortex system would be substantially greater. This sensitivity of the aero-optic environment to the precise helicopter flow field emphasizes the need for full-scale experimental data.

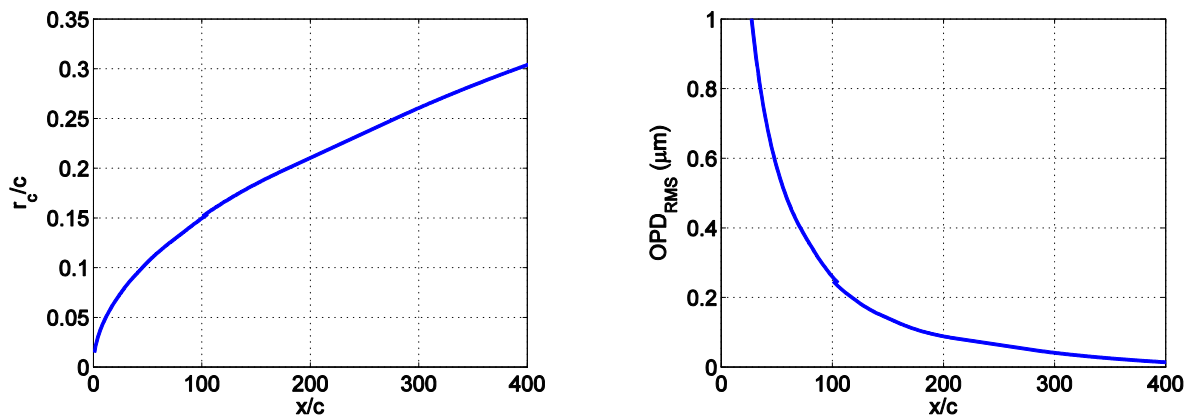


**Fig. 15. Predicted core radius and  $\text{OPD}_{\text{RMS}}$  as a function of distance from the tip of a UH-60 helicopter blade for a  $0.254 \text{ m}$  aperture.**

## IV. Concluding Remarks

The aberrations due to helicopter tip vortices originate from the index-of-refraction variations associated with the reduced pressure and density at the vortex core. A scaling relation has been developed from basic fluid-mechanic equations and calibrated using the Lamb-Oseen vortex model in conjunction with a thermodynamic model, the weakly compressible model (WCM). Using this calibrated relation, the tip-vortex aberrations for a realistic case have been shown to be sufficiently strong to significantly impair the performance of an optical system mounted below the body of a typical helicopter.

Future efforts will be directed at confirming the results obtained thus far. These efforts will consist of additional experimental measurements in a high-speed wind tunnel with lower model blockage. Furthermore, the flowfield around a helicopter in different flight regimes will be carefully analyzed to better define the aero-optic environment associated with different flight modes.

## Acknowledgements

These efforts were sponsored by the Office of Naval Research under Award Number N00014-07-1-0291. The U.S. Government is authorized to reproduce and distribute reprints for governmental purposes notwithstanding any copyright notation thereon.

## References

- [1] Gordeyev, S., and Jumper, E.J., "Aero-Optical Characteristics of Compressible Subsonic Turbulent Boundary Layers," AIAA-2003-3606, June, 2003.
- [2] Rennie, R. M., Siegenthaler, J. P., and Jumper, E. J., "Forcing of a Two-Dimensional, Weakly-Compressible Subsonic Free Shear Layer," AIAA 2006-0561, Jan., 2006.
- [3] Gordeyev, S., Hayden, T., and Jumper, E., "Aero-Optical and Flow Measurements Over a Flat-Windowed Turret," *AIAA Journal*, Vol. 45, No. 2, 2007, pp.347-357.
- [4] Gordeyev, S., Post, M.L., McLaughlin, T., Ceniceros, J., and Jumper, E.J., "Aero-Optical Environment Around a Conformal-Window Turret," *AIAA Journal*, Vol. 45, No. 7, 2007, pp.1514-1524.
- [5] Rennie, R.M., Duffin, D.A., and Jumper, E. J., "Characterization and Aero-Optic Correction of a Forced Two-Dimensional, Weakly-Compressible Subsonic Free Shear Layer," *AIAA Journal*, Vol. 46, No. 11, 2008, pp.2787-2795.
- [6] Devenport, W., Rife, M., Stergios, L., and Gordon, F., "The structure and development of a wing-tip vortex", *J Fluid Mech* (1996) 326:67-106.
- [7] Iungo, G., Skinner, P., and Buresti, G., "Correction of wandering smoothing effects on static measurements of a wing-tip vortex", *Exp Fluids* (2009) 46:435-452.
- [8] Green, S. I. and Acosta, A. J., "Unsteady flow in trailing vortices," *J Fluid Mech* (1991) 227:107-134.
- [9] Rossow, V. J., "Lift-generated vortex wakes of subsonic transport air," *Progress in Aerospace Sciences* (1999) 35: 507-660.
- [10] Zang, H.J., Zhou, Y., Whitelaw, J.H., "Near-Field Wing-Tip Vortices and Exponential Vortex Solution," *J Aircraft* (2006), Vol. 43, 2:445-449.
- [11] Papamoschou, D., and Roshko, A., "The compressible turbulent shear layer: an experimental study," *Journal of Fluid Mechanics*, Vol. 197, 1988, pp. 453-477.
- [12] Fitzgerald, E.J. and Jumper, E.J., "The Optical Distortion Mechanism in a Nearly Incompressible Free Shear Layer," *Journal of Fluid Mechanics*, 512, 2004, pp. 153-189.
- [13] Babie, B. M., "An Experimental and Analytical Study of the Stability of Counter-Rotating Vortex Pairs with Applications for Aircraft Wake Turbulence Control," Ph.D. Dissertation, Aerospace and Mechanical Engineering Department, Univ. of Notre Dame, Notre Dame, IN, April 2008.
- [14] Leishman, J. G., "Principles of Helicopter Aerodynamics," Cambridge Aerospace Series (2000).
- [15] Gordeyev, S. and Jumper, E., "Aero-Optics Characteristics of Compressible, Subsonic Turbulent Boundary Layers," 34<sup>th</sup> AIAA Plasma Dynamics and Lasers Conference, 2003, AIAA 2003-3606.
- [16] Siegenthaler, J., Gordeyev, S., and Jumper, E. J., "Shear Layers and Aperture Effects for Aero Optics," AIAA-2005-4772, June, 2005.
- [17] Siegenthaler, J., "Guidelines for Adaptive-Optic Correction Based on Aperture Filtration," Ph.D. Dissertation, Aerospace and Mechanical Engineering Department, Univ. of Notre Dame, Notre Dame, IN, December 2008.